RSC Advances

PAPER

View Article Online
View Journal | View Issue

Cite this: *RSC Adv.*, 2023, **13**, 8464

Efficient photo-assisted Fenton-like reaction of yolk–shell CuSe(Cu_2Se)/g-C_3N_4 heterojunctions for methylene blue degradation†

ChangSheng Liu and ShaoLin Xue *

Herein, a CuSe(Cu_2Se) yolk–shell structure (CC) was synthesized when room temperature was 25 degree Celsius using Cu_2O as a soft template, and the g-C_3N_4/CuSe(Cu_2Se) heterojunction (CC-G) was formed by coupling appropriate amounts of g-C_3N_4 in the selenization process to provide a novel, green, economical, and efficient photo-Fenton catalytic material. Photo-Fenton degradation experiments proved that in the presence of hydrogen peroxide (H_2O_2), a small amount of g-C_3N_4 hybridization on Cu-based Fenton catalysts significantly improved methylene blue (MB) degradation. The suitable amount of g-C_3N_4 hybridization was selected according to the degradation efficiency. The mass of g-C_3N_4 constituted 20% of the mass of the Cu_2O soft template. The composite material prepared using this combination (CC-G-20) exhibited the best MB degradation performance. The MB degradation efficiency in the CC-G-20/H_2O_2/visible light system was almost 98.3% after 60 min, which is higher than those of the parent materials (g-C_3N_4, 12.7%; CC, 58.6%) and had cyclic stability. The catalytic system can also stably degrade MB under dark conditions, where the MB degradation was almost 82% after 60 min. The heterojunction prevented excessive electrons and holes (e^- and h^+) recombination, stabilizing the reactive active substance of hydroxyl in the photo-Fenton-like catalytic system. Electron paramagnetic resonance and photoluminescence experiments confirmed this inference.

Received 29th December 2022
Accepted 5th March 2023

DOI: 10.1039/d2ra08309d

rsc.li/rsc-advances

1. Introduction

Dye pollution from the textile industry has become an increasingly serious environmental problem. According to statistics, nearly 200 billion liters of hardy biodegradable colored wastewater are produced every year.[1,2] These discharged polluting dyes can seriously harm human health and all levels of natural ecosystems.[3] Moreover, the self-purification capacity of the environment is insufficient to treat these dyes in a short time. Therefore, the artificial construction of efficient catalytic systems can reduce such natural burden.

In this regard, many efficient photocatalysts, such as TiO_2, MoS_2, Bi_2MoO_6, and Fe_2O_3, have been successfully developed.[4–7] Another technology used to degrade pollutants is Fenton oxidation, which is a branch of advanced oxidation technology. Compared with traditional photocatalytic systems, some Fenton-like oxidation can efficiently degrade pollutants under dark conditions.[8] Moreover, photo-Fenton oxidation technology improves some of the defects of Fenton oxidation technology as it has higher degradation efficiency, requires less chemical additives, and produces less sludge.[3] In addition to iron, Fenton-like systems composed of some transition metals and hydrogen peroxide have also been extensively studied. Some Fenton-like catalytic systems, such as CuS[9,10] and CuSe,[11] can well solve the continuous catalytic degradation of pollutants within 24 h.

Copper selenide is a wideband p-type semiconductor[11] with unique thermoelectric,[21] Seebeck,[22] and photo-electric[23] effects and is widely applied to solar cells[24] because of adjustable stoichiometric ratios (CuSe, Cu_2Se, Cu_3Se_2, and $Cu_{2-x}Se$)[12–15] and different types of crystallographic systems: cubic, tetragonal, single monocline, and hexagonal structures.[16–20] In addition, copper selenide quantum dots have been used in traditional photocatalysis because of their high specific surface area, crystallinity, and small particle size.[25] Similar to traditional iron ions, copper ions generate highly active hydroxyl radicals (˙OH) by reacting with hydrogen peroxide (H_2O_2).[26,27] ˙OH plays an important role in the degradation of pollutants.[28] Therefore, copper selenide can be regarded as an excellent Fenton-like catalyst with the synergistic action of light and H_2O_2. In the presence of H_2O_2, $Cu_{2-x}Se$ thin film catalysts can remove methylene blue (MB) from the water after visible light irradiation.[29] Copper selenide materials with different morphologies and sizes can effectively degrade organic dyes in coordination with visible light and H_2O_2.[11,30,31] This efficient Fenton-like photocatalytic system induced by visible light

College of Science, Donghua University, Shanghai, China. E-mail: 18321325227@163.com; slxue@dhu.edu.cn

† Electronic supplementary information (ESI) available. See DOI: https://doi.org/10.1039/d2ra08309d

avoids strict pH conditions and it is more green and efficient with low energy consumption.[32–34]

Furthermore, visible-light-driven g-C_3N_4-based photocatalytic systems have broad application prospects in wastewater purification.[35] Photocatalytic systems with g-C_3N_4 entail low costs and can be combined with many metal and nonmetal materials, thereby significantly improving the photocatalytic efficiency of the system.[36,37] The improvement of the visible light activity of g-C_3N_4-based catalysts mainly stems from their good visible light response, high chemical stability, strong redox ability, and rapid charge transfer and separation processes.[38] The surface modification of g-C_3N_4 catalysts can effectively improve the photocatalytic decomposition of water.[39] g-C_3N_4 coupled with other catalysts can effectively reduce the recombination of photogenerated electrons and holes.[40]

The above two semiconductor types have excellent properties and are easy to prepare. If they are coupled at a specific proportion, the recombination of photoinduced carriers may be effectively reduced, thus improving the synergistic catalytic degradation of visible light and H_2O_2.

Herein, we report a novel composite of g-C_3N_4 hybridized CuSe(Cu_2Se) as an effective Fenton-like photocatalyst for MB degradation. In the preparation of copper selenide at 25 degrees Celsius, g-C_3N_4 was successfully hybridized with the CuSe(Cu_2Se) yolk–shell structure. A little g-C_3N_4 was added during the selenization of the Cu_2O soft template. The ratios of the usage of g-C_3N_4 and Cu_2O soft template are different (Section 2.2.3). Finally, CC-G-20 was used as the main research object because it has the best MB degradation ability obtained at different g-C_3N_4 dosages. Whether other excessive metallic chalcogenide compounds rational hybridize g-C_3N_4 by this method to improve the catalytic level, and it is also worth discussing how to make g-C_3N_4/Fenton catalytic materials obtain the most appropriate hybrid g-C_3N_4 way (the most effective degradation of dyes).

CC-G-20 composites were characterized *via* X-ray diffraction (XRD), transmission electron microscopy (TEM), Fourier transform infrared spectroscopy (FT-IR), X-ray photoelectron spectroscopy (XPS), and ultraviolet-visible spectroscopy (UV-vis). The active substances involved in the materials/visible light/H_2O_2 synergistic system were investigated through photoluminescence (PL) and electron paramagnetic resonance (EPR). The cycling stability of the CC-G-20 composites was studied. After the fourth cycle experiment, the degradation efficiency of MB by CC-G-20 reached 96.3% within 120 min. The MB degradation performance and possible reaction mechanism of the synergistic system were described.

In direct Fenton-like reaction under dark conditions, H_2O_2 reacts directly with Cu(I) to form the Fenton reactive active $^{\bullet}OH$. Moreover, photoinduced Fenton-like reaction and direct Fenton-like reaction simultaneously occur under light conditions. In the CuSe/g-C_3N_4 heterojunction structure, which promotes the separation of photogenerated electrons and holes in the local area of the shell, the electrons then react with the H_2O_2 to form $^{\bullet}OH$. Combining the above two processes, the degradation efficiency of MB is improved.

2. Experimental

2.1. Chemicals

The chemical reagents used in this experiment were analytically pure (Aladdin Shanghai), including sodium sulfite (Na_2SO_3), sodium hydroxide (NaOH) and selenium powder (Se), copper sulfate pentahydrate ($CuSO_4 \cdot 5H_2O$), polyvinyl pyrrolidone (PVP-K30), ascorbic acid ($C_6H_8O_6$), anhydrous ethanol (C_2H_6O), ethylene glycol (EG, $(CH_2OH)_2$), and melamine ($C_3N_3(NH_2)_3$).

2.2. Synthesis of CuSe(Cu_2Se)/g-C_3N_4

2.2.1. Synthesis of g-C_3N_4. Graphite-phase carbon nitride (g-C_3N_4) was synthesized through heat treatment. We placed 5 g of $C_3N_3(NH_2)_3$ into a ceramic boat and kept it fluffy and smooth. Then, we placed the ceramic boat into a tubular furnace. The furnace temperature was raised from 25 degrees Celsius to 550 degrees Celsius at a rate of 15 degree Celsius per 1 min. Calcination was continued at 550 degrees Celsius for 4 h. After the tubular furnace cooled to 25 degrees Celsius, the obtained sample (g-C_3N_4) was placed into an agate mortar for manual grinding. After 1 h, the resulting faint yellow powder was collected and properly stored for subsequent use.

2.2.2. Synthesis of the Cu_2O soft template and selenium water. The CuSe(Cu_2Se) yolk–shell structure was prepared through cuprous oxide reaction with solution containing selenium ions at 25 degree Celsius. First, 1 g of $CuSO_4 \cdot 5H_2O$ was dissolved in 100 mL of deionized water. Then, 0.2 g of PVP-K30 was added to form solution A, and 4 g of NaOH was dissolved in 50 mL of deionized water to form solution B. Solution B was quickly added to solution A using a dropper and stirred for 30 min. Then, 3 mmol of $C_6H_8O_6$ was added to the mixture and stirred vigorously for 10 min. The orange product (Cu_2O) was washed thrice with deionized water and C_2H_6O, respectively. After centrifugation, it was dried at 60 degree Celsius for 12 h in an oven.

Second, 1.5 mmol of Na_2SO_3 was dissolved in 18 mL of deionized water, and 0.15 mol of NaOH was added to the solution. After NaOH was completely dissolved, 1.5 mmol of Se powder was added and stirred for 10 min. Then, the beaker was placed into an oil bath, heated to 80 degree Celsius, and stirred for 30 min, forming a wine-red solution containing selenium ions.

2.2.3. Synthesis of CuSe(Cu_2Se)(CC)/g-C_3N_4 yolk–shell. For solution C, 20 mg of Cu_2O was placed in 12 mL of EG and then ultrasonically dispersed for 30 min. A certain amount of g-C_3N_4 was placed in 3 mL selenium water for ultrasonic dispersion. During dispersion, g-C_3N_4 deposited at the bottom of the container was shaken well by hand every 5 min, placed in solution C after 30 min, and stirred vigorously at 25 degrees Celsius for 100 min to obtain a black product—the CuSe(Cu_2Se)(CC) yolk–shell material. Then, the obtained product was washed with deionized water and C_2H_6O twice. Following centrifugation, it was dried at 60 degree Celsius for 12 h in an oven. The composite of g-C_3N_4 and Cu_2O according to different mass ratios was named CC-G-*X*, $X = 5$, 10, 20, 30 (*X*/100:the mass of g-C_3N_4/the mass of Cu_2O).

2.3. Characterization

The crystal structures of the materials were characterized *via* XRD (Bruker D8 ADVANCE). The surface microstructures of the materials were observed using a field-emission scanning electron microscope FESEM (Hitachi S-4800). Scanning transmission electron microscopy (STEM, TALOS F200X) was used to observe the interior structure of composites and the distribution of the main elements. XPS (Escalab 250Xi) was used to analyze the chemical environment information of the materials. The valence band (VB)–XPS diagram of the CC material was measured using XPS (Thermo Scientific K-Alpha), and the approximate VB position was determined. A Fourier infrared microscopic imaging spectrometer (NicoletIn10MX/Nicolet6700) was used to characterize the functions of the composites. $BaSO_4$ was used as a reference background, and a UV-vis spectrophotometer (Shimadzu UV-3600) was used to measure the absorption spectrum of the materials. A UV-vis spectrophotometer (Beijing Purkinge TU-1810) was used to measure the MB concentration. Electron spin resonance (EPR) signals were measured in visible light using a Bruker EMXPLUS paramagnetic resonance spectrometer. The PL spectra of the prepared samples were obtained using the QM/TM spectrometer of American PTI.

2.4. Photocatalytic degradation experiments

MB degradation in the CC-G-*X*/visible light/H_2O_2 system was measured at 25 degrees Celsius. The photocatalytic reaction instrument was used in the experiment (Shanghai Bilang). The details are as follows. First, 10 mg of the studied sample was placed in a cylindrical quartz tube. Then, 25 mL of an MB aqueous solution was added (30 mg L^{-1} concentration). Post dispersion, it was placed in a dark box to simulate a photocatalytic reaction and stirred in darkness at 25 degree Celsius for 60 min. After the sample and dye solution reached adsorption analytical equilibrium (The adsorption properties are shown in Table 1 of the supplementary document.†), 0.1 mL of H_2O_2 was dripped into the tube, and a xenon lamp was turned on. The xenon lamp was located in the center, surrounded by eight quartz reactors. The 420 nm UV cutoff filter was located between the light source and the quartz reactor. Then, 2 mL of the samples was drawn every 20 min, and the lamp was switched off after 120 min. Each sample was immediately centrifuged for 1 min using an 11 000 rpm high-speed centrifuge. After two cycles of centrifugation, the supernatant was extracted, and the dye concentration in the solution was detected using a UV-vis spectrophotometer at the characteristic wavelength of 664 nm.

2.5. Analysis experiment

EPR signals were measured under vis light using a Bruker EMXPLUS paramagnetic resonance spectrometer. First, 30 μg of the sample was added to 200 mM of deionised water, followed by the addition of 30 μL of DMPO (Add TEMPO when testing the signal of the holes, other conditions remain the same), and the resulting mixture was rapidly mixed. A capillary tube was used to absorb a certain amount of the mixed liquid, which was then dropped into a quartz tube and placed into the EPR sample chamber for the hydroxyl radical test. Spot UV-vis light (420 nm UV cut-off filter) was used as the light source. The signals were recorded every 5 min.

3. Results and discussion

3.1. Characterization

XRD patterns of the CC-G-20 composite, CC, and g-C_3N_4 are shown in Fig. 1(a). Fig. 1(b) shows the full diffraction spectrum of the CC and CC-G-20 materials. The XRD spectra of CC and CC-G-20 exhibited peaks corresponding to the following angles: 26.4°, 27.8°, 31.1°, 45.9°, 49.9°, and 56.5°, which corresponded to the (1 1 1), (1 1 2), (0 0 6), (2 0 0), (1 1 8), and (2 0 6) crystal planes, respectively (JCPDS card number 34-0171). The corresponding cell parameters of the standard card were $a = b =$ 3.940 Å and $c = 17.230$ Å, corresponding to the hexagonal crystal structure of CuSe. In addition, at 26.5°, 44.8°, and 53.2°, three high diffraction peaks did not correspond to the above JCPDS cards. These three peaks corresponded to the (1 1 1) and (2 2 0) crystal planes of Cu_2Se (standard JCPDS card no. 88-2043), and the cell parameters were $a = b = c = 5.694$ Å, corresponding to the cubic crystal structure of Cu_2Se. These results show that CC was an impure phase. A wide diffraction peak was observed at about 27.6°, a strong wide peak corresponding to the crystal plane of g-C_3N_4 (0 0 2). This was caused by the superposition of the conjugate aromatic system.[41] The diffraction peak of CC-G-20 at 27.6° was not obvious, which was because the content of g-C_3N_4 in actual hybridization is low.[1,42]

The TEM photos clearly show the specific internal microstructures of the samples. Fig. 2(a and b) clearly shows the yolk–shell structure of the composite material (CC-G-20). The diameter of CC-G-20 was about 1.5–2 μm, and the diameter of the yolk was about 1 μm. The thickness of the shell part was less than 100 nm. More g-C_3N_4 was obviously attached to the shell. Fig. 2(c–h) shows the distribution of elements in the composites, mainly C, N, O, Se, and Cu. Because of the use of carbon film during the test, the distribution of C was relatively uniform. Most of the N was concentrated on the surface of the spherical shell. O elements were the oxygen absorbed into the material. Cu and Se were mainly distributed in the shell and yolk regions. Fig. 2(i–j) shows the TEM pictures of g-C_3N_4 and CC.

We tested the XPS spectra of CC-G-20 and its precursor material CC to further characterize their chemical environment information. As shown in Fig. 3(a), Cu, Se, C, and N elements mainly exist in CC-G-20. However, no characteristic peak corresponding to N was observed in CC because no g-C_3N_4 existed in CC. Fig. 3(b and c) are the fine spectra of C and N in CC-G-20, respectively. The sp^2 bond of the C atom (N–C=N), and the adventitious carbon species (C–C) on g-C_3N_4 were located at 288.3 and 284.8 eV, respectively (Fig. 3(b)).[43] The chemical states of carbide was located at 282.2 eV.[44] In Fig. 3(c), N exhibited three distinct peaks, and the peak at 398.8 eV corresponded to the sp^2-specific orbital of nitrogen atoms (C=N–C),[45] whereas the peaks at 400.5 and 404.9 eV are related to the amino groups carrying hydrogen (C–N–H) and charge effect localization in

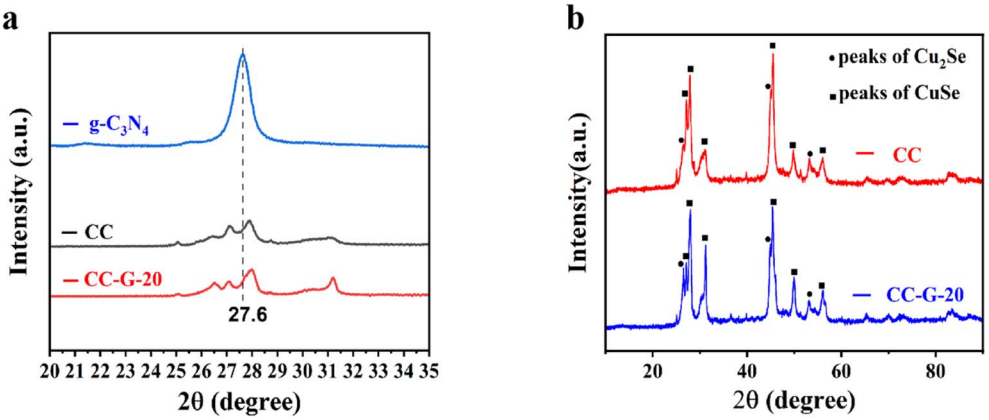

Fig. 1 (a) Magnified XRD patterns of the CC, g-C_3N_4 and CC-G-20. (b) The full diffraction spectrum of CC and CC-G-20.

heterocyclic rings.[46] In Fig. 3(d), the peaks at 932.1 eV (CC and CC-G-20) corresponded to Cu $2p_{3/2}$ of Cu^{2+}, whereas the peaks at 952.1 (CC) and 952.0 eV (CC-G-20) are related to the spin–orbit splitting effect of Cu $2p_{1/2}$, and satellite peaks appearing at 944.2 (CC) and 945.9 eV (CC-G-20). Furthermore, the peaks located at 933.9 and 954.1 eV (CC) and 933.1 and 953.1 eV (CC-G-20) correspond to Cu $2p_{3/2}$ and Cu $2p_{1/2}$ of Cu^{+}.[47] These data also confirm the existence of Cu^{+} in the materials. As shown in Fig. 3(e), The Se $3d_{5/2}$ and Se $3d_{3/2}$ were located at 54.2 and 54.9 eV, respectively(CC-G-20: 53.9 and 54.8 eV).[48]

FT-IR analysis was performed for g-C_3N_4 in the CC-G composite shell. CC-G-20 with the best catalytic performance and its two parent materials CC and g-C_3N_4 were selected. Their FT-IR spectra are shown in Fig. 4. The absorption of the CN-heterocyclic system at 1250, 1319, 1463, 1575, and 1630 cm^{-1} could be attributed to its typical stretching patterns.[49] The peak between 3000 and 3500 cm^{-1} originated from the N–H of the g-C_3N_4 structure.[50] The characteristic absorption peak of g-C_3N_4 at 812 cm^{-1} was caused by the stretching vibration of the triazine cycle.[51] CuSe(Cu_2Se) (CC) had no peak at 812 cm^{-1}; however, CC-G-20 exhibited a small peak, which was not obvious because of the low content of g-C_3N_4 in the complex.[1,42]

The light absorption properties of the prepared g-C_3N_4 and CC were tested from 250 to 800 nm using a UV-vis spectrometer. As presented in Fig. 5(a), the as-synthesized CuSe(Cu_2Se) yolk–shell (CC) exhibits strong light absorption at the visible light range because of its narrow band gap. Moreover, absorption at less than 450 nm is due to the band gap of g-C_3N_4.[52] The

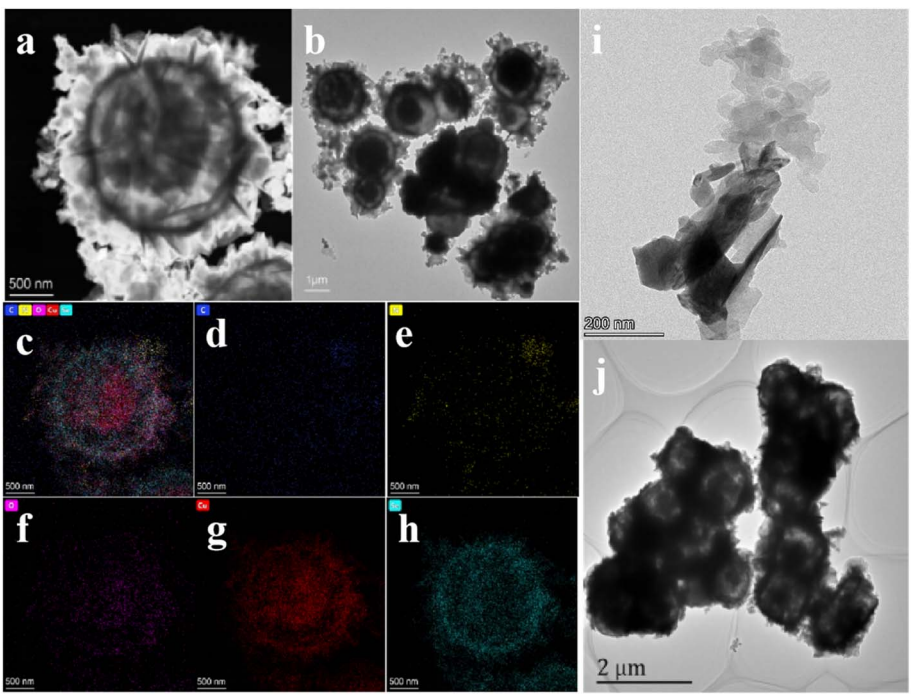

Fig. 2 TEM images of (a and b) CC-G-20; (c–h) HAADF images of CC-G-20; (i) g-C_3N_4; (j) CC.

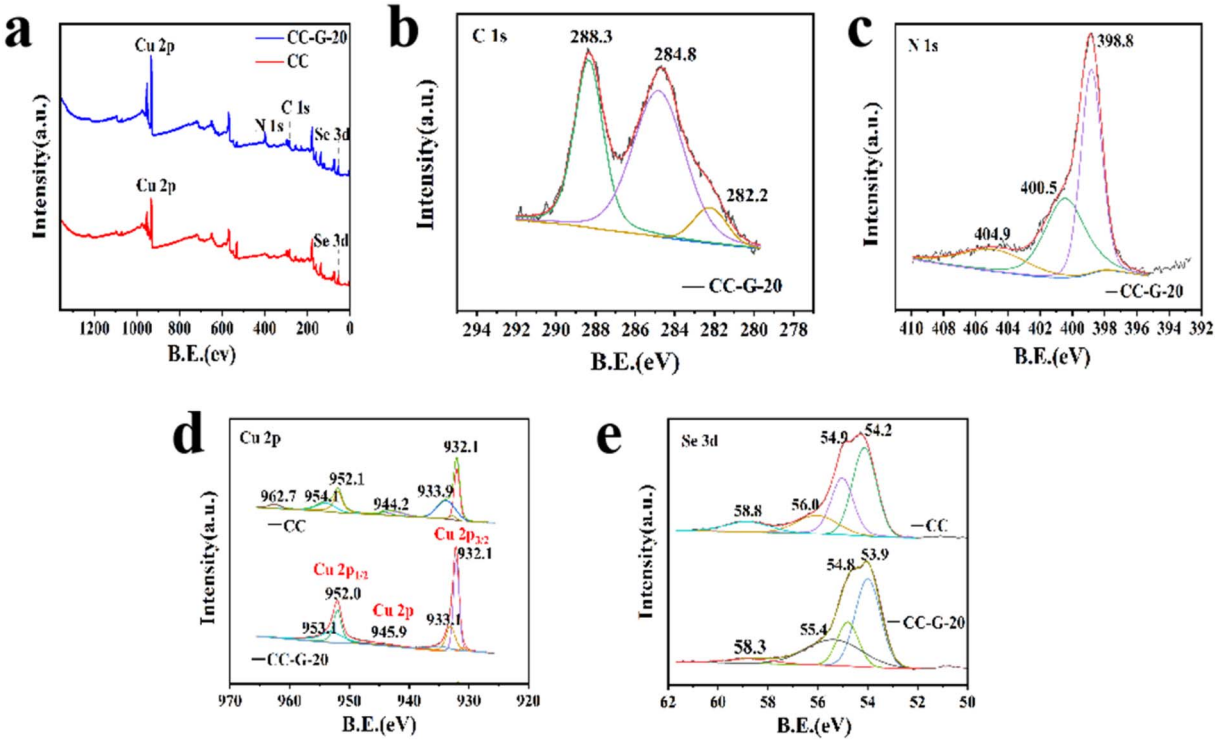

Fig. 3 XPS spectra of CC-G-20 referred to the parent CC. (a) Survey scan, (b) C 1s, (c) N 1s, (d) Cu 2p, and (e) Se 3d.

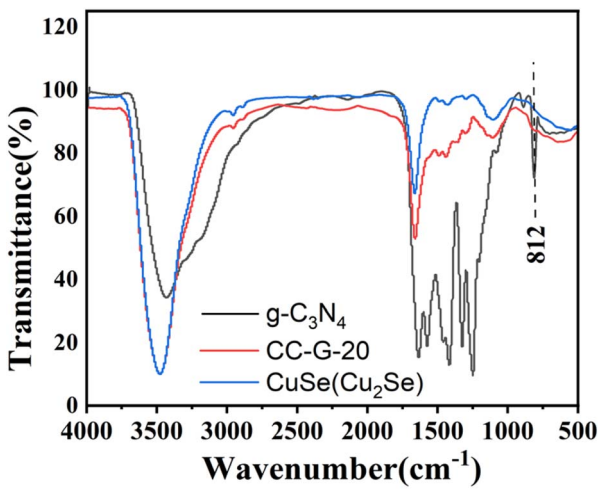

Fig. 4 FT-IR spectra of the CC, g-C_3N_4, and CC-G-20 composites.

absorption property of CC-G-20 is between those of CC and g-C_3N_4.

The band gap energy (E_g) is estimated using light absorption images and the Tauc plot approach using eqn (1).[53]

$$K(hv - E_g)^{1/n} = F(R)hv \quad (1)$$

Herein, $F(R)$ is the absorption coefficient; n represents the type of semiconductor; K is a constant; hv is the light energy, and E_g is the band gap energy. Fig. 5(b) and (c) show the band gap of CC and g-C_3N_4 as 1.41 and 2.68 eV, respectively. The calculated band gap of CC is considerably smaller than that of the most reported CuSe structures.[54]

3.2. MB degradation of the CC-G composites

A TU-1810 UV-vis spectrophotometer was used to measure the change in MB solution concentration with reaction time to calculate the photocatalytic efficiency (C/C_0) of the materials in a certain reaction time. We found the following order of photocatalytic efficiency: CC-G-20 > CC-G-30 > CC-G-10 > CC-G-5 > CC > g-C_3N_4. Among the composites, CC-G-30 and CC-G-10 had similar MB degradation levels, which were lower than the degradation level of CC-G-20 but higher than the degradation level of CC-G-5. Results show that the catalytic efficiency of CC-G-20 with a small amount of g-C_3N_4 was considerably higher than those of the single CC and g-C_3N_4, regardless of the high or low load of g-C_3N_4. The CC-G-20/visible light/H_2O_2 system had the highest catalytic efficiency after 120 min, almost reaching 100% (Fig. 6(a)), which was confirmed in the UV-vis absorption spectral variation of MB in Fig. 6(d). After 60 min of reaction, the MB degradation efficiency of CC-G-20 reached 98.3% (Fig. 6(b)). It can be observed that g-C_3N_4 and CuSe on the surface of the composite materials had synergistic effects on improving MB degradation. Significantly higher degradation efficiency may be the cause of g-C_3N_4 and CC heterojunction, which substantially reduces the recombination rate of photogenic electrons and photogenic holes. Thus, more isolated electrons and holes are generated, which contribute to the generation of $^{\bullet}OH$. $^{\bullet}OH$ is the active substance of pollutant degradation in Fenton-like reactions. Too little g-C_3N_4 may

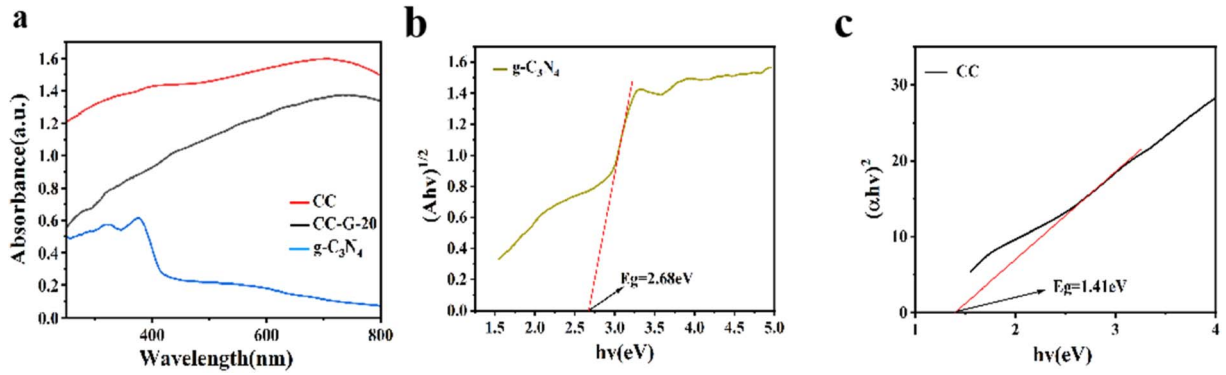

Fig. 5 (a) UV-vis spectra of CC-G-20 referred to the parent CC and g-C_3N_4. (b) Band gap width of g-C_3N_4 (plots of $(h\nu)^{1/2}$ *vs.* photon energy [$h\nu$]). (c) Band gap width of CC (plots of $(h\nu)^2$ *vs.* photon energy [$h\nu$]).

result in the excessive recombination of photogenerated carriers compared with CC-G-20. When more g-C_3N_4 is compounded onto the CC material, too much load is exerted owing to the local "covering effect".[55] In both cases, the MB degradation efficiency of the system is reduced (Fig. 6(a)). Therefore, the recombination amount of g-C_3N_4 in the process of material synthesis must be controlled. Following several tests, we determined that CC-G-20 eventually reaches the optimal MB degradation level.

Further, the effects of three variables (CC-G-20/visible light/H_2O_2) on the degradation efficiency of MB in the system were studied. As shown in Fig. 6(c), the visible light stability of the MB dye in an aqueous solution without catalysts and H_2O_2 was verified through a blank control experiment. Under visible light, when H_2O_2 was added without a catalyst, the degradation rate reached 41% within 120 min, which proved that H_2O_2 could mildly degrade MB under visible light. In the absence of H_2O_2, CC-G-20 had a low degradation efficiency of pollutants (only 13% after 120 min). CC-G-20 had a certain ability to degrade MB in the presence of H_2O_2 under dark conditions, and the degradation rate was 82% after 60 min. Therefore, the composite material can also be effectively applied under practical light conditions. Under visible light, the degradation efficiency of CC-G-20 was further improved, which was close to 98.3% after 60 min. At each sampling time point, the MB degradation level of the CC-G-20/visible light/H_2O_2 system was

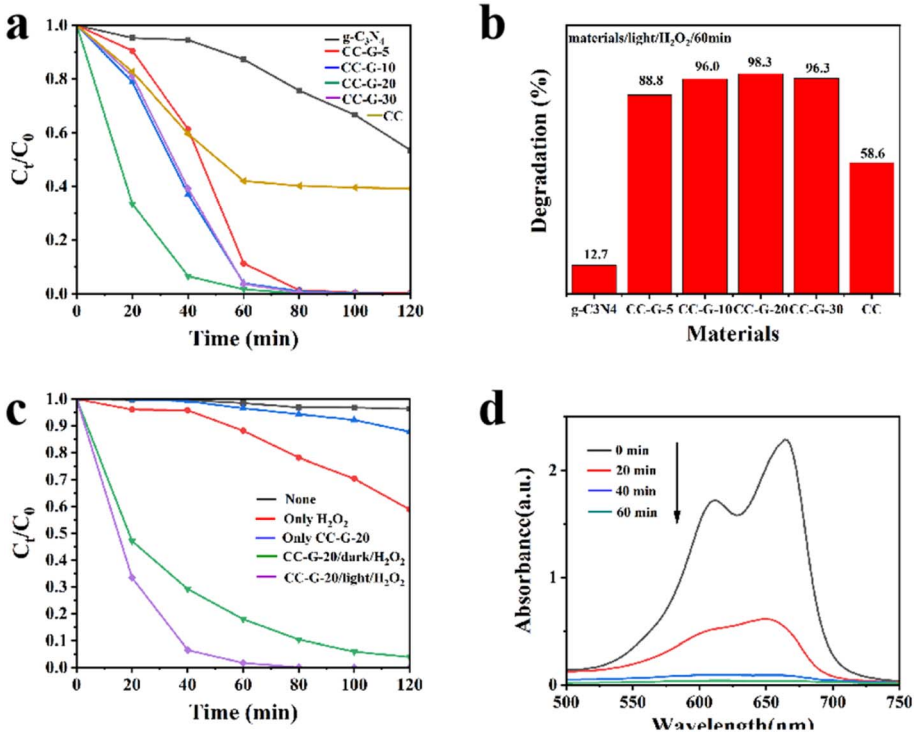

Fig. 6 Reaction conditions: 10 mg of photocatalyst, 25 mL of 30 mg L^{-1} MB^{-1}, 0.1 mL of H_2O_2. (a and c) Degradation of MB under different conditions. (b) MB degradation efficiencies of CC-G-*X*, g-C_3N_4, and CC at 60 min. (d) UV-vis spectral changes of MB with time (CC-G-20).

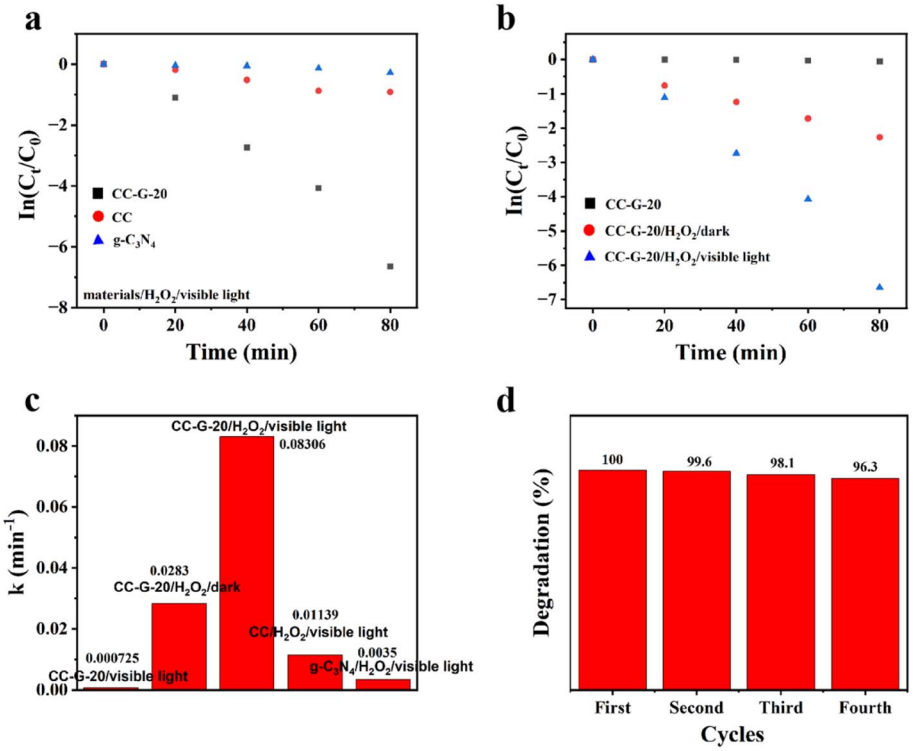

Fig. 7 (a and b) $\ln(C_t/C_0)$ of different catalytic systems (CC-G-20, CC, and g-C_3N_4/visible light/H_2O_2 systems) varied with the reaction time. (c) Reaction rate constants of five catalytic systems in 7(a and b). (d) CC-G-20/visible light/H_2O_2 cycle experiment for MB degradation.

better than that of the CC-G-20/dark/H_2O_2 system. This was because light further promoted the separation of carriers in the catalytic process. The above results indicate that visible light, H_2O_2, and CC-G composites all play important roles in MB degradation. Apparently, the synergistic effect of the three elements maximized the MB degradation efficiency.

We performed linear fitting on the MB photodegradation kinetics curve ($\ln(C/C_0) = kT$) to further quantify the above synergistic effects. k is the slope after the linear fitting of the scatter points in Fig. 7(a and b), and it is the rate constant of the materials/H_2O_2/visible light system. The higher the k value, the greater the MB degradation promotion effect of the system. The k values of the three catalytic oxidation systems ([CC-G-20, CC, and g-C_3N_4]/visible light/H_2O_2) were calculated as 0.08306, 0.01139, and 0.0035, respectively. Furthermore, the k values of the three systems (CC-G-20/H_2O_2/dark; CC-G-20/H_2O_2/visible light; and CC-G-20/visible light) were calculated as 0.0283, 0.08306, and 0.000725, respectively. These k values are summarized in Fig. 7(c). The synergy coefficient SI[56] is further quoted: $SI = k_{MVH}/(k_{MH} + k_{MV})$, where k_{MVH}, k_{MV}, and k_{MH} are the rate constants of CC-G-20/visible light/H_2O_2, CC-G-20/visible light, and CC-G-20/dark/H_2O_2, respectively. The calculated result of SI is 2.86. These results indicate that this work hybridized primitive materials (CC and g-C_3N_4) with the general performance of MB degradation to form a composite material (CC-G-20) with excellent collaborative catalytic efficiency and

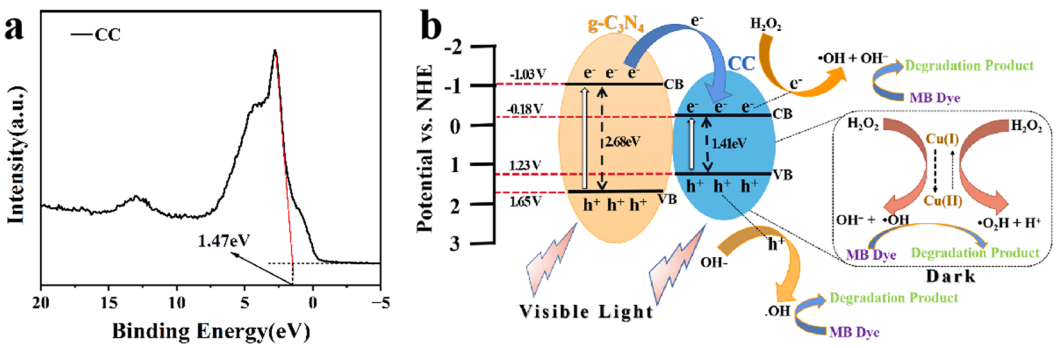

Fig. 8 (a) Spectrum of the valence band XPS. (b) Band structure of CC-G-20; schematic illustration of the photocatalytic reaction of CC-G-20 and the degradation of MB over CC-G-20 under dark and light irradiation conditions.

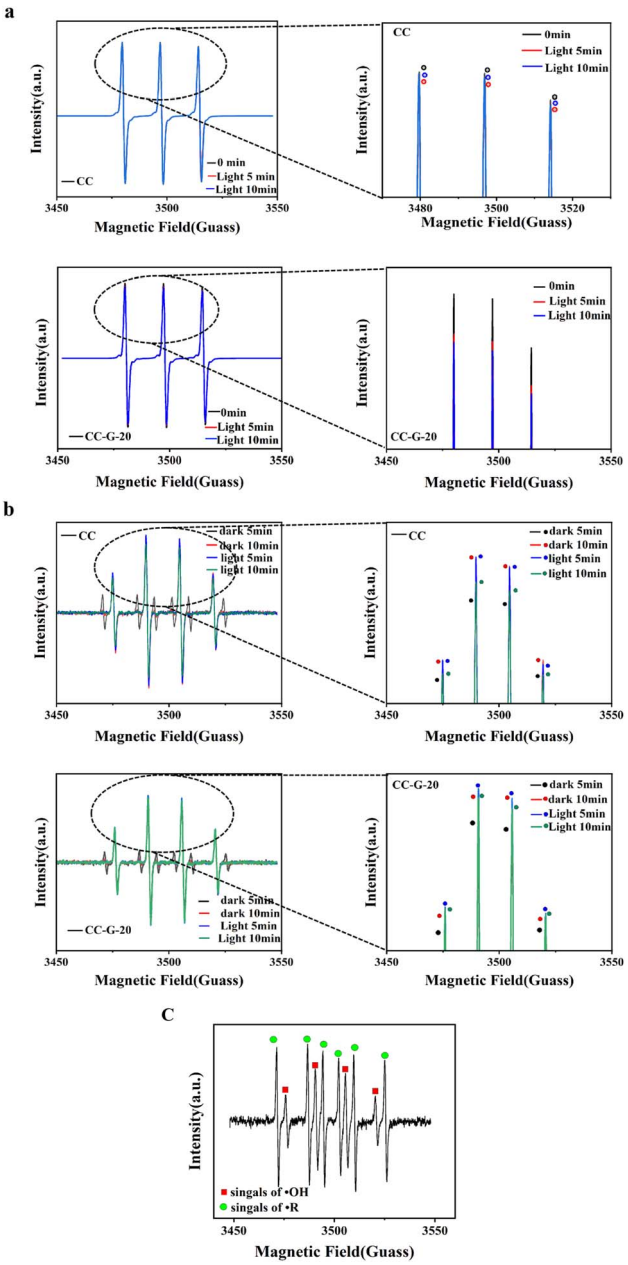

Fig. 9 (a) EPR spectra of TEMPO-h^+ adducts formed with the irradiation time of visible light (dark) in the CC and CC-G-20 suspension. (b) EPR spectra of DMPO–•OH adducts formed with the irradiation time of visible light (dark) in the suspension of CC and CC-G-20. (c) EPR spectra of CC-G-20 without H_2O_2.

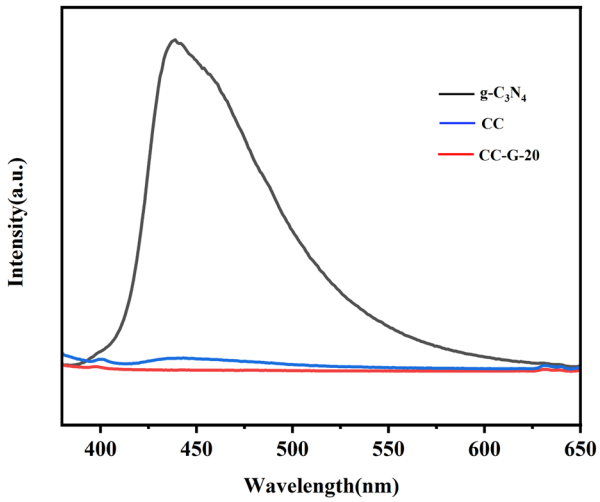

Fig. 10 PL emission spectra of CC, g-C_3N_4, and CC-G-20.

that can efficiently and sustainably degrade MB under either visible light or dark conditions. Further details in this regard are discussed hereafter. Fig. 7(d) shows the ability of the synergistic system to degrade MB after four test cycles. The catalytic efficiency was 96.5% at 120 min after four cycles. This proves the cyclic stability of CC-G-20.

3.3. Proposed photocatalytic mechanism

The band structure of the CC-G-20 composite was determined using the VB–XPS spectrum (Fig. 8(a)) and Tauc plot spectrum (Fig. 5(b and c)). The VB position of the CC is at approximately 1.47 eV (~1.23 eV *vs.* normal hydrogen electrode [NHE]), as shown in Fig. 8(b), whereas the VB of g-C_3N_4 is at approximately 1.65 eV *vs.* NHE.[57] Moreover, the bandgaps of CC and g-C_3N_4 are at approximately 1.41 and 2.68 eV, respectively, according to the UV-differential reflectance spectroscopy in Fig. 5(b and c). The CB positions of CC and g-C_3N_4 could be calculated as −0.18 and −1.03 eV, respectively. The band structure of the prepared CC-G-20 is presented in Fig. 8(b). The redox potential for H_2O/•OH is 2.80 eV.[58] These results imply that the photogenerated holes cannot react with the absorbed H_2O molecule to form •OH. However, according to the results of the degradation experiments, adding H_2O_2 can solve this problem.

•OH formed *via* H_2O_2 excitation can be quantified using EPR, employing DMPO as a trapping reagent. The generation of photo-generated holes can be determined by the reduction of the EPR signal of TEMPO because photo-generated holes consume TEMPO under illumination. Fig. 9(a) indicates that the number of generated holes increases with increasing illumination time for the CC-G-20/H_2O_2/vis light system; the formation of holes increases under light irradiation for 5 min compared to that in the dark at 0 min, and the number of holes decreases after 10 min of light irradiation compared to that after 5 min. These results indicate that the isolated photo-generated holes and electrons in CC-G-20 are more stable than those in CC with increasing illumination time. These electrons can further react with H_2O_2 to form •OH and OH− (Fig. 8), enhancing the efficiency and stability of MB degradation. Fig. 9(b) shows •OH signals. The •R signal at the initial stage of the reaction is caused by the residual solvent (EG) on the materials (The •R signal in Fig. 9(c) is also for this reason), which gradually disappears with the progress of the reaction. •OH signal intensities of CC/H_2O_2/vis light and CC-G-20/H_2O_2/vis light systems increase with an increase in the reaction time under dark conditions. Under light irradiation for 10 min, the •OH signal of the CC/H_2O_2/vis light system is weak, whereas that of the CC-G-20/H_2O_2/vis light system remains stable. This is confirmed by the change in the signal of photo-generated holes,

as shown in Fig. 9(a). Fig. 9(c) shows a weak $^{\bullet}OH$ signal of CC-G-20 without H_2O_2, which is weaker than that in the system with H_2O_2. This confirms the experimental results shown in Fig. 6(c).

Fig. 10 shows that CC-G-20 exhibits a lower PL emission peak intensity than CC and g-C_3N_4. This indicates that the reorganisation of photo-generated carriers in CC-G-20 is significantly inhibited because g-C_3N_4 and CC form a heterojunction in the composite.[59] Therefore, this composite can achieve a significant separation of electrons and holes. Photo-generated electrons are transferred from g-C_3N_4 to the CC yolk–shell structure during the photo-Fenton reaction, implying that the system can produce more sustainable and stable $^{\bullet}OH$. This is consistent with the results of the EPR analysis.

Based on the above-mentioned results, the mechanism of MB degradation by CC-G-20/H_2O_2 can be discussed. Fig. 8 indicates that the degradation process can be analysed in two stages. A small amount of H_2O_2 reacts with copper ions in the material to produce reactive $^{\bullet}OH$ in the dark. The produced $^{\bullet}OH$ degrade pollutants and is accompanied by the redox cycle of Cu^{+}/Cu^{2+}. Following conjectures can be drawn using eqn (2) and (3):[60] (i) Cu^{+} reacts with H_2O_2 to generate Cu^{2+}; (ii) Cu^{2+} is converted to Cu^{+} as shown in eqn (3) with the generation of $^{\bullet}O_2H$ radicals. (i) And (ii) are accompanied by the formation of $^{\bullet}OH$. Hydroxyl radicals react with pollutants to form minerals [eqn (4)].[61] The same process occurs under light irradiation.

$$Cu^{+} + H_2O_2 \rightarrow Cu^{2+} + {}^{\bullet}OH + OH^{-} \quad (2)$$

$$Cu^{2+} + H_2O_2 \rightarrow Cu^{+} + {}^{\bullet}O_2H + H^{+} \quad (3)$$

$$MB + {}^{\bullet}OH \rightarrow \text{intermediate products} \rightarrow CO_2 + H_2O \quad (4)$$

$^{\bullet}OH$ generated by the reaction of photo-generated holes with water is negligible on exposing CC-G-20 to light (without H_2O_2). CC-G-20 with a small amount of H_2O_2 absorbs light energy under vis light to generate holes and electrons. Photo-generated holes and electrons are distributed at the top of the VB and the bottom of the CB of g-C_3N_4 and CC, respectively. H_2O_2 reacts with the photo-generated electrons of CC to generate $^{\bullet}OH$ [eqn (5)] to degrade MB. The separated holes on the surface of CC can react with OH^{-} to generate $^{\bullet}OH$ [eqn (6)].[52] The total number of $^{\bullet}OH$ produced by the two methods enables the CC-G-20/H_2O_2/vis light system to achieve the highest MB degradation efficiency.

$$e^{-} + H_2O_2 \rightarrow {}^{\bullet}OH + OH^{-} \quad (5)$$

$$OH^{-} + h^{+} \rightarrow {}^{\bullet}OH \quad (6)$$

4. Conclusions

Here, highly active photo-Fenton catalytic materials (CuSe(Cu_2Se)/g-C_3N_4[CC-G]) were prepared at 25 degrees Celsius. CC-G-*X* indicates that the mass of g-C_3N_4 accounted for *X*% of the mass of the Cu_2O soft template. Under dark conditions, CC-G-20 exhibited good MB degradation ability in the presence of a small amount of H_2O_2. Minimum or excess amounts of g-C_3N_4 in the composites reduced the degree of MB degradation. The MB degradation rate by CC-G-20 was further improved under vis light irradiation. The MB degradation rate by CC-G-20 was ~100% after 120 min (98.3% after 60 min), which was considerably higher than those of g-C_3N_4 and CC. For achieving the optimal performance, approximately 0.1 mL of H_2O_2 was used per 25 mL (30 mg L^{-1-1}) of the MB aqueous solution. This reaction did not consume significant amounts of H_2O_2, thereby reducing reagent costs. The results show that g-C_3N_4 hybridised successfully on the yolk–shell structure of CC to form the CC-G heterojunction. This material with a novel structure and high cycle stability exhibits excellent performance in the photo-Fenton degradation of MB. The strategy of hybridising CC with a small amount of g-C_3N_4 proposed herein can be extended to study the hybridisation of copper selenide with other materials. The hybridisation of CC with appropriate amounts of g-C_3N_4 reduced the recombination of electrons and holes. Moreover, two-dimensional g-C_3N_4 provides more reactive sites,[61] thereby promoting the Fenton-like excitation of H_2O_2. This study demonstrated that a small amount of g-C_3N_4 hybridised with CC can effectively improve the photo-Fenton catalytic performance of Cu-based materials.

Conflicts of interest

There are no conflicts to declare.

References

1 X. Y. Li, Y. H. Pi, L. Q. Wu, Q. B. Xia, J. L. Wu, Z. Li and J. Xiao, Facilitation of the visible light-induced Fenton-like excitation of H_2O_2 *via* heterojunction of g-C_3N_4/NH_2-Iron terephthalate metal-organic framework for MB degradation, *Appl. Catal., B*, 2017, **202**, 653–663, DOI: 10.1016/j.apcatb.2016.09.073.

2 S. Dhaarani, A. K. Priya, T. V. Rajan and D. N. Kartic, Degradation of various dyes using laccase enzyme, *J. Environ. Sci. Eng.*, 2012, **54**, 489–494.

3 A. Tkaczyk, K. Mitrowska and A. Posyniak, Synthetic organic dyes as contaminants of the aquatic environment and their implications for ecosystems: a review, *Sci. Total Environ.*, 2020, **717**, 137222, DOI: 10.1016/j.scitotenv.2020.137222.

4 S. X. Min, J. H. Hou, Y. G. Lei, X. H. Ma and G. X. Lu, Facile one-step hydrothermal synthesis Toward strongly coupled TiO_2/graphene quantum dots photocatalysts for efficient hydrogen evolution, *Appl. Surf. Sci.*, 2017, **396**, 1375–1382, DOI: 10.1016/j.apsusc.2016.11.169.

5 B. Han and Y. H. Hu, MoS_2 as a co-catalyst for photocatalytic hydrogen production from water, *Energy Sci. Eng.*, 2016, **4**, 285–304, DOI: 10.1002/ese3.128.

6 Q. He, Y. H. Ni and S. Y. Ye, Heterostructured Bi_2O_3/Bi_2MoO_6 nanocomposites: simple construction and enhanced visible-light photocatalytic performance, *RSC Adv.*, 2017, **7**, 27089–27099, DOI: 10.1039/C7RA02760E.

7 P. Cai, S. M. Zhou, D. K. Ma, S. N. Liu, W. Chen and S. M. Huang, Fe_2O_3-modified porous $BiVO_4$ nanoplates

with enhanced photocatalytic activity, *Nano-Micro Lett.*, 2015, **7**, 183–193, DOI: 10.1007/s40820-015-0033-9.

8 Y. Ma, J. Zhang, Y. Wang, Q. Chen, Z. Feng and T. Sun, Concerted catalytic and photocatalytic degradation of organic pollutants over CuS/g-C_3N_4 catalysts under light and dark conditions, *J. Adv. Res.*, 2019, **16**, 135–143, DOI: 10.1016/j.jare.2018.10.003.

9 Z. Y. Wang, A. von dem Bussche, P. K. Kabadi, A. B. Kane and R. H. Hurt, Biological and environmental transformations of copper-based nanomaterials, *ACS Nano*, 2013, **7**, 8715–8727, DOI: 10.1021/nn403080y.

10 L. Guo, K. L. Zhang, X. X. Han, Q. Zhao, D. J. Wang and F. Fu, In-plane CuS/Bi_2WO_6 p–n heterostructures with promoted visible-light-driven Photo-Fenton degradation performance, *Nanomaterials*, 2019, **9**, 9, DOI: 10.3390/nano9081151.

11 Y. T. Mao, H. Y. Zou, Q. Wang and C. Z. Huang, Large-scale preparation of fernwort-like single-crystalline superstructures of CuSe as Fenton-like catalysts for dye decolorization, *Sci. China: Chem.*, 2016, **59**, 903–909, DOI: 10.1007/s11426-016-5600-5.

12 M. L. Yao, W. S. Liu, X. Chen, Z. S. Ren, S. Wilson, Z. F. Ren and C. Opeil, Low temperature thermoelectric properties of p-type copper selenide with Ni, Te and Zn dopants, *J. Alloys Compd.*, 2017, **699**, 718–721, DOI: 10.1016/j.jallcom.2016.12.400.

13 S. Deka, A. Genovese, Y. Zhang, K. Miszta, G. Bertoni, R. Krahne, C. Giannini and L. Manna, Phosphine-free synthesis of p-type copper(I) selenide nanocrystals in hot coordinating solvents, *J. Am. Chem. Soc.*, 2010, **132**, 8912–8914, DOI: 10.1021/ja103223x.

14 W. Cao, Z. Y. Wang, L. Miao, J. Shi and R. Xiong, Thermoelectric properties of strained beta-Cu_2Se, *ACS Appl. Mater. Interfaces*, 2021, **13**, 34367–34373, DOI: 10.1021/acsami.1c08686.

15 S. L. Liu, R. Wang, Q. T. Wang, Q. H. Tian and X. Cui, A facile synthesis of $Ni_{0.85}Se$@$Cu_{2-x}Se$ nanorods as high-performance supercapacitor electrode materials, *Dalton Trans.*, 2021, **50**, 13543–13553, DOI: 10.1039/d1dt02199k.

16 B. Pejjai, V. R. M. Minnam Reddy, T. R. R. Kotte and C. Park, Facile and eco-friendly synthesis of water-soluble $Cu_{2-x}Se$ nanoparticles for photovoltaic applications, *Mater. Sci. Semicond. Process.*, 2020, **112**, DOI: 10.1016/j.mssp.2020.105013.

17 P. Huang, Y. F. Kong, Z. M. Li, F. Gao and D. X. Cui, Copper selenide nanosnakes: bovine serum albumin-assisted room temperature controllable synthesis and characterization, *Nanoscale Res. Lett.*, 2010, **5**, 949–956, DOI: 10.1007/s11671-010-9587-0.

18 B. Yu, W. Liu, S. Chen, H. Wang, H. Wang, G. Chen and Z. Ren, Thermoelectric properties of copper selenide with ordered selenium layer and disordered copper layer, *Nano Energy*, 2012, **1**, 472–478, DOI: 10.1016/j.nanoen.2012.02.010.

19 S. H. Jin and Y. S. Lim, Effect of Zn-doping on the phase transition behavior and thermoelectric transport properties of Cu_2Se, *Korean J. Met. Mater.*, 2020, **58**, 466–471, DOI: 10.3365/KJMM.2020.58.7.466.

20 Y. Q. Liu, F. X. Wang, Y. Xiao, H. D. Peng, H. J. Zhong, Z. H. Liu and G. B. Pan, Facile microwave-assisted synthesis of klockmannite CuSe nanosheets and their exceptional electrical properties, *Sci. Rep.*, 2014, **4**, 5998, DOI: 10.1038/srep05998.

21 X. Q. Chen, Z. Li, J. P. Yang, Q. Sun and S. X. Dou, Aqueous preparation of surfactant-free copper selenide nanowires, *J. Colloid Interface Sci.*, 2015, **442**, 140–146, DOI: 10.1016/j.jcis.2014.11.052.

22 D. Byeon, R. Sobota, K. Delime-Codrin, S. Choi, K. Hirata, M. Adachi, M. Kiyama, T. Matsuura, Y. Yamamoto, M. Matsunami and T. Takeuchi, Discovery of colossal Seebeck effect in metallic Cu2Se, *Nat. Commun.*, 2019, **10**, 72, DOI: 10.1038/s41467-018-07877-5.

23 D. C. Jordan, S. R. Kurtz, K. VanSant and J. Newmiller, Compendium of photovoltaic degradation rates, *Prog. Photovolt.: Res. Appl.*, 2016, **24**, 978–989, DOI: 10.1002/pip.2744.

24 X. Q. Chen, Y. Bai, Z. Li, L. Z. Wang and S. X. Dou, Ambient synthesis of one-/Two-dimensional CuAgSe ternary nanotubes as counter electrodes of quantum-dot-sensitized solar cells, *ChemPlusChem*, 2016, **81**, 414–420, DOI: 10.1002/cplu.201500466.

25 K. Kaviyarasu, A. Ayeshamariam, E. Manikandan, J. Kennedy, R. Ladchumananandasivam, U. U. Umbelino Gomes, M. Jayachandran and M. Maaza, Solution processing of CuSe quantum dots: photocatalytic activity under RhB for UV and visible-light solar irradiation, *Mater. Sci. Eng., B*, 2016, **210**, 1–9, DOI: 10.1016/j.mseb.2016.05.002.

26 A. D. Bokare and W. Choi, Review of iron-free Fenton-like systems for activating H_2O_2 in advanced oxidation processes, *J. Hazard. Mater.*, 2014, **275**, 121–135, DOI: 10.1016/j.jhazmat.2014.04.054.

27 S. Hussain, E. Aneggi and D. Goi, Catalytic activity of metals in heterogeneous Fenton-like oxidation of wastewater contaminants: a review, *Environ. Chem. Lett.*, 2021, **19**, 2405–2424, DOI: 10.1007/s10311-021-01185-z.

28 W. Liu, Z. Ai and L. Zhang, Design of a neutral three-dimensional electro-Fenton system with foam nickel as particle electrodes for wastewater treatment, *J. Hazard. Mater.*, 2012, **243**, 257–264, DOI: 10.1016/j.jhazmat.2012.10.024.

29 A. Ghosh, C. Kulsi, D. Banerjee and A. Mondal, Galvanic synthesis of $Cu_{2-X}Se$ thin films and their photocatalytic and thermoelectric properties, *Appl. Surf. Sci.*, 2016, **369**, 525–534, DOI: 10.1016/j.apsusc.2016.02.020.

30 W. W. Wang, L. J. Zhu, P. Z. Lv, J. F. Li and X. W. Zhao, Facile synthesis of Cu_3Se_2/Cu_2Se/Cu2O hollow microspheres by sacrificial template method at room temperature and excellent photodegradation activity, *Mater. Res. Bull.*, 2019, **110**, 190–197, DOI: 10.1016/j.materresbull.2018.10.029.

31 X. W. Wang, X. Y. Zhong, H. L. Lei, Y. H. Geng, Q. Zhao, F. Gong, Z. J. Yang, Z. L. Dong, Z. Liu and L. Cheng, Hollow Cu_2Se nanozymes for tumor photothermal-catalytic therapy, *Chem. Mater.*, 2019, **31**, 6174–6186, DOI: 10.1021/acs.chemmater.9b01958.

32 A. D. Bokare and W. Choi, Review of iron-free Fenton-like systems for activating H_2O_2 in advanced oxidation processes, *J. Hazard. Mater.*, 2014, **275**, 121–135, DOI: 10.1016/j.jhazmat.2014.04.054.

33 X. Li, Y. Pi, Q. Xia, Z. Li and J. Xiao, TiO_2 encapsulated in salicylaldehyde-NH_2−MIL-101(Cr) for enhanced visible light-driven photodegradation of MB, *Appl. Catal., B*, 2016, **191**, 192–201, DOI: 10.1016/j.apcatb.2016.03.034.

34 M. Su, C. He, V. K. Sharma, M. Abou Asi, D. Xia, X. Z. Li, H. Deng and Y. Xiong, Mesoporous zinc ferrite: synthesis, characterization, and photocatalytic activity with H_2O_2/visible light, *J. Hazard. Mater.*, 2012, **211–212**, 95–103, DOI: 10.1016/j.jhazmat.2011.10.006.

35 S. M. Yin, J. Y. Han, T. H. Zhou and R. Xu, Recent progress in g-C_3N_4 based low cost photocatalytic system: activity enhancement and emerging applications, *Catal. Sci. Technol.*, 2015, **5**, 5048–5061, DOI: 10.1039/C5CY00938C.

36 I. F. Teixeira, E. C. M. Barbosa, S. C. E. Tsang and P. H. C. Camargo, Carbon nitrides and metal nanoparticles: from controlled synthesis to design principles for improved photocatalysis, *Chem. Soc. Rev.*, 2018, **47**, 7783–7817, DOI: 10.1039/c8cs00479j.

37 S. W. Cao, J. X. Low, J. Yu and M. Jaroniec, Polymeric photocatalysts based on graphitic carbon nitride, *Adv. Mater.*, 2015, **27**, 2150–2176, DOI: 10.1002/adma.201500033.

38 X. B. Li, J. Xiong, X. M. Gao, J. T. Huang, Z. J. Feng, Z. Chen and Y. F. Zhu, Recent advances in 3D g-C_3N_4 composite photocatalysts for photocatalytic water splitting, degradation of pollutants and CO_2 reduction, *J. Alloys Compd.*, 2019, **802**, 196–209, DOI: 10.1016/j.jallcom.2019.06.185.

39 J. J. Yi, W. El-Alami, Y. H. Song, H. M. Li, P. M. Ajayan and H. Xu, Emerging surface strategies on graphitic carbon nitride for solar driven water splitting, *Chem. Eng. J.*, 2020, **382**, DOI: 10.1016/j.cej.2019.122812.

40 C. Prasad, H. Tang and I. Bahadur, Graphitic carbon nitride based ternary nanocomposites: from synthesis to their applications in photocatalysis: A recent review, *J. Mol. Liq.*, 2019, **281**, 634–654, DOI: 10.1016/j.molliq.2019.02.068.

41 H. Xu, J. Yan, Y. G. Xu, Y. H. Song, H. M. Li, J. X. Xia, C. J. Huang and H. L. Wan, Novel visible-light-driven AgX/graphite-like C_3N_4(X = Br, I) hybrid materials with synergistic photocatalytic activity, *Appl. Catal., B*, 2013, **129**, 182–193, DOI: 10.1016/j.apcatb.2012.08.015.

42 X. X. Yang, W. Y. Xin, X. H. Yin and X. Shao, Enhancement of photocatalytic activity in reducing CO_2 over CdS/g-C_3N_4 composite catalysts under UV light irradiation, *Chem. Phys. Lett.*, 2016, **651**, 127–132, DOI: 10.1016/j.cplett.2016.03.027.

43 H. X. Fang, H. Guo, C. G. Niu, C. Liang, D. W. Huang, N. Tang, H. Y. Liu, Y. Y. Yang and L. Li, Hollow tubular graphitic carbon nitride catalyst with adjustable nitrogen vacancy: enhanced optical absorption and carrier separation for improving photocatalytic activity, *Chem. Eng. J.*, 2020, **402**, 126185, DOI: 10.1016/j.cej.2020.126185.

44 J. Zhao, E. G. Garza, K. Lam and C. M. Jones, Comparison study of physical vapor-deposited and chemical vapor-deposited titanium nitride thin films using X-ray photoelectron spectroscopy, *Appl. Surf. Sci.*, 2000, **158**, 246–251, DOI: 10.1016/S0169-4332(00)00024-6.

45 L. Ge, C. C. Han, J. Liu and Y. Li, Enhanced visible light photocatalytic activity of novel polymeric g-C_3N_4 loaded with Ag nanoparticles, *Appl. Catal., A*, 2011, **409–410**, 215–222, DOI: 10.1016/j.apcata.2011.10.006.

46 W. X. Zou, B. Deng, X. Hu, Y. Zhou, Y. Pu, S. Yu, K. Ma, J. Sun, H. Wan and L. Dong, Crystal-plane-dependent metal oxide-support interaction in CeO_2/g-C_3N_4 for photocatalytic hydrogen evolution, *Appl. Catal., B*, 2018, **238**, 111–118, DOI: 10.1016/j.apcatb.2018.07.022.

47 H. Y. Liu, W. Ruan, Z. Zhang, F. H. Shen, Y. M. Zhou and H. M. Yang, Dual 2-dimensional CuSe/g-C_3N_4 nano-heterostructure for boosting immobilization of elemental mercury in flue gas, *Chem. Eng. J.*, 2022, **435**, 134696, DOI: 10.1016/j.cej.2022.134696.

48 Q. Yang, Z. Yang, H. Li, J. Zhao, J. Yang, W. Qu and K. Shih, Selenide functionalized natural mineral sulfides as efficient sorbents for elemental mercury capture from coal combustion flue gas, *Chem. Eng. J.*, 2020, **398**, 125611, DOI: 10.1016/j.cej.2020.125611.

49 Q. Liu, Y. Guo, Z. Chen, Z. Zhang and X. Fang, Constructing a novel ternary Fe(III)/graphene/g-C_3N_4 composite photocatalyst with enhanced visible-light driven photocatalytic activity *via* interfacial charge transfer effect, *Appl. Catal., B*, 2016, **183**, 231–241, DOI: 10.1016/j.apcatb.2015.10.054.

50 Y. J. Meng, L. X. Zhang, H. F. Jiu, Q. L. Zhang, H. Zhang, W. Ren, Y. Sun and D. T. Li, Construction of g-C_3N_4/ZIF-67 photocatalyst with enhanced photocatalytic CO_2 reduction activity, *Mater. Sci. Semicond. Process.*, 2019, **95**, 35–41, DOI: 10.1016/j.mssp.2019.02.010.

51 Y. Guo, R. X. Wang, P. Wang, Y. Li and C. Wang, Developing polyetherimide/graphitic carbon nitride floating photocatalyst with good photodegradation performance of methyl orange under light irradiation, *Chemosphere*, 2017, **179**, 84–91, DOI: 10.1016/j.chemosphere.2017.03.085.

52 H. Chen, L. Qiu, J. Xiao, S. Ye, X. Jiang and Y. Yuan, Inorganic-organic hybrid NiO-g-C_3N_4 photocatalyst for efficient methylene blue degradation using visible light, *RSC Adv.*, 2014, **4**, 22491–22496, DOI: 10.1039/c4ra01519c.

53 G. T. Urs, R. V. Hurkadli, R. V. Basavaraj, M. Niranjana, A. Manjunath and R. Somashekar, Study of optical and conducting properties of $FeCl_3$ doped PVA polymers, *Prog. Cryst. Growth Charact. Mater.*, 2014, **60**, 87–93, DOI: 10.1016/j.pcrysgrow.2014.09.003.

54 H. B. Chen, Y. J. Xing, S. T. Liu, J. L. Fu, H. L. Shi, Y. J. Liang, L. J. Wang and W. Z. Wang, Efficient pollutant degradation under ultraviolet to near-infrared light irradiation and dark condition using CuSe nanosheets: mechanistic insight into degradation, *J. Colloid Interface Sci.*, 2022, **613**, 103–116, DOI: 10.1016/j.jcis.2022.01.020.

55 J. Jin, J. Yu, D. Guo, C. Cui and W. Ho, A hierarchical Z-scheme CdS-WO_3 photocatalyst with enhanced CO_2 reduction activity, *Small*, 2015, **11**, 5262–5271, DOI: 10.1002/smll.201500926.

56 L. Ai, C. Zhang, L. Li and J. Jiang, Iron terephthalate metal-organic framework: revealing the effective activation of hydrogen peroxide for the degradation of organic dye under visible light irradiation, *Appl. Catal., B*, 2014, **148–149**, 191–200, DOI: **10.1016/j.apcatb.2013.10.056**.

57 S. G. Meng, X. F. Ning, T. Zhang, S. F. Chen and X. L. Fu, What is the transfer mechanism of photogenerated carriers for the nanocomposite photocatalyst Ag_3PO_4/g-C_3N_4, band-band transfer or a direct Z-scheme?, *Phys. Chem. Chem. Phys.*, 2015, **17**, 11577–11585, DOI: **10.1039/c5cp01523e**.

58 W. Jiang, X. Wang, Z. Wu, X. Yue, S. Yuan, H. Lu and B. Liang, Silver oxide as superb and stable photocatalyst under visible and near-infrared light irradiation and its photocatalytic mechanism, *Ind. Eng. Chem. Res.*, 2015, **54**, 832–841, DOI: **10.1021/ie503241k**.

59 G. Gao, Y. Jiao, F. Ma, Y. Jiao, E. Waclawik and A. Du, Carbon nanodot decorated graphitic carbon nitride: new insights into the enhanced photocatalytic water splitting from ab initio studies, *Phys. Chem. Chem. Phys.*, 2015, **17**, 31140–31144, DOI: **10.1039/c5cp05512a**.

60 Z. Li, L. W. Mi, W. H. Chen, H. W. Hou, C. T. Liu, H. L. Wang, Z. Zheng and C. Y. Shen, Three-dimensional CuS hierarchical architectures as recyclable catalysts for dye decolorization, *CrystEngComm*, 2012, **14**, 3965–3971, DOI: **10.1039/c2ce00018k**.

61 M. Nouri, N. Zare-Dehnavi, F. Jamali-Sheini and R. Yousefi, Synthesis and characterization of type-II p(Cu_xSe_y)/n(g-C_3N_4) heterojunction with enhanced visible-light photocatalytic performance for degradation of dye pollutants, *Colloids Surf., A*, 2020, **595**, 124656, DOI: **10.1016/j.colsurfa.2020.124656**.